Photo-evaporation of Globulettes

Numerical hydrodynamic studies of photo-evaporating low-mass globules in the Rosette Nebula

Master Thesis

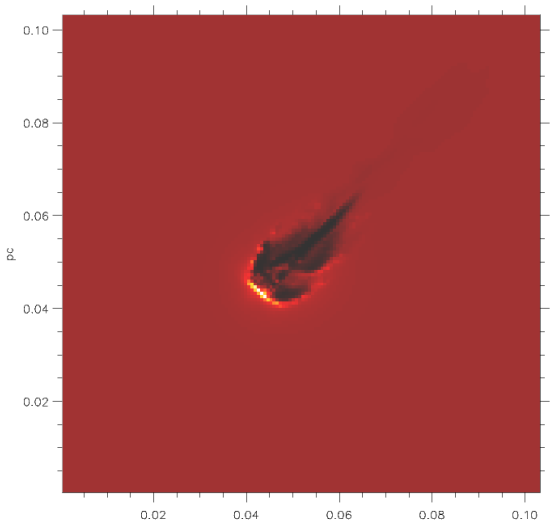

Andrej Kuutmann
Department of Astronomy, Stockholm University
Supervised by Dr. Garrelt Mellema

October 10, 2007

Abstract

In this work, the long-term evolution of *globulettes*, low-mass globules found in H II regions, is studied through numerical hydrodynamic simulations. It has been proposed by Gahm et al. (2007) that these clouds may form free-floating planetary mass objects due to shock compression, caused by heating from the intense UV radiation of the central OB star cluster. To address this possibility, lifetimes are calculated for three different 3D simulated cases, similar to globulettes found in the Rosette Nebula. A plane-parallel approximation of the radiation field is used, as well as an inhomogeneous initial density distribution. The ionizing radiation will cause the globulettes to photo-evaporate, creating a rocket acceleration effect from the mass ejected on the heated side of the cloud. For a typical globulette with an initial mass of 29.5 M_{Jup} a lifetime of 5×10^4 yrs is estimated. This estimate is compared to the analytical models of Mellema et al. (1998) and Bertoldi & McKee (1990) which suggest longer lifetimes; the discrepancy is attributed to fragmentation of the clouds in the numerical simulation, which is not adequately described by the models. Synthesized Hα images and lightcurves are presented, indicating that the bright rims of small clouds are only likely to be visible in dim parts of the Rosette Nebula. The morphology of simulated clouds generally agrees with observations. While the code does not include self-gravity, the gravitational stability of the clouds is studied indirectly. It is concluded that clouds in the planetary mass range are stable against gravitational collapse, from supporting thermal pressure alone, when in pressure equilibrium with the heated ionization front. However, gravitation may play a significant role during the initial shock compression.

Contents

1 Introduction

Stars are born within dense, cold molecular clouds, forming in local high density knots as a result of gravitational instability of the clouds. Under the typical conditions in these clouds, hundreds or thousands of solar masses of cloud material are needed in order for the cloud to become gravitationally unstable, exceeding the criterion known as the Jeans mass. The spontaneous mechanism of star formation, through a simultaneous process of accretion and fragmentation, favors the creation of a cluster of massive OB stars. Once these hot and luminous stars are born, they produce large amounts of UV photons energetic enough to ionize the surrounding cloud, creating an ionization front moving outwards from the central star cluster. Observationally, the H II region created by the cluster appears as a hot, bright, roundish nebula. It is surrounded by a shell of cold, dusty gas which appears dark against the background.

When the ionization front moves through a molecular cloud of inhomogeneous mass distribution, high density regions will tend to resist ionization longer, leading to the formation of structures such as pillars and trunks. It is presently thought that these structures, while being eroded away due to the ionization and heating, can eventually form detached clouds within the H II region. These are known as globules.

Globules appear as dark against the bright background and are found in various sizes, broadly classified according to size and morphology (Leung, 1985). The smallest category of these clouds have been categorized by Grenman (2006) and Gahm et al. (2007) as *globulettes*, constituting a pronounced peak in the lower range of the size distribution. Effectively, the observed lower cutoff in the distribution of the size of this class of objects is set by the observational limitations. Based on high resolution surveys in mainly the Rosette Nebula and IC 1805 (Figure 1), 173 globulettes were found, with a majority having an estimated mass below 13 Jupiter masses. They appear elliptical or teardrop shaped, sometimes with visible bright rims facing the central cluster. The authors also discussed the possibility that these objects may form free floating planetary mass objects, concluding that globulettes might become gravitationally unstable (Gahm et al., 2007). Reipurth et al. (2003) have observed similar small globules scattered around Thackeray's globules in the NGC 2944 H II region, estimating them to be very short lived and consequently not star forming. De Marco et al. (2006) analyzed a large number of HST imaged H II regions in search for protoplanetary disks, also addressing the possibility of star formation in molecular cloud fragments.

Bertoldi (1989) and Bertoldi & McKee (1990) formulated an approximate analytical theory of interstellar clouds photo-evaporating due to the intense ionizing radiation of a newly formed star in two related papers, extending upon the earlier work of Oort and Spitzer (1955) and Dyson (1968, 1973).

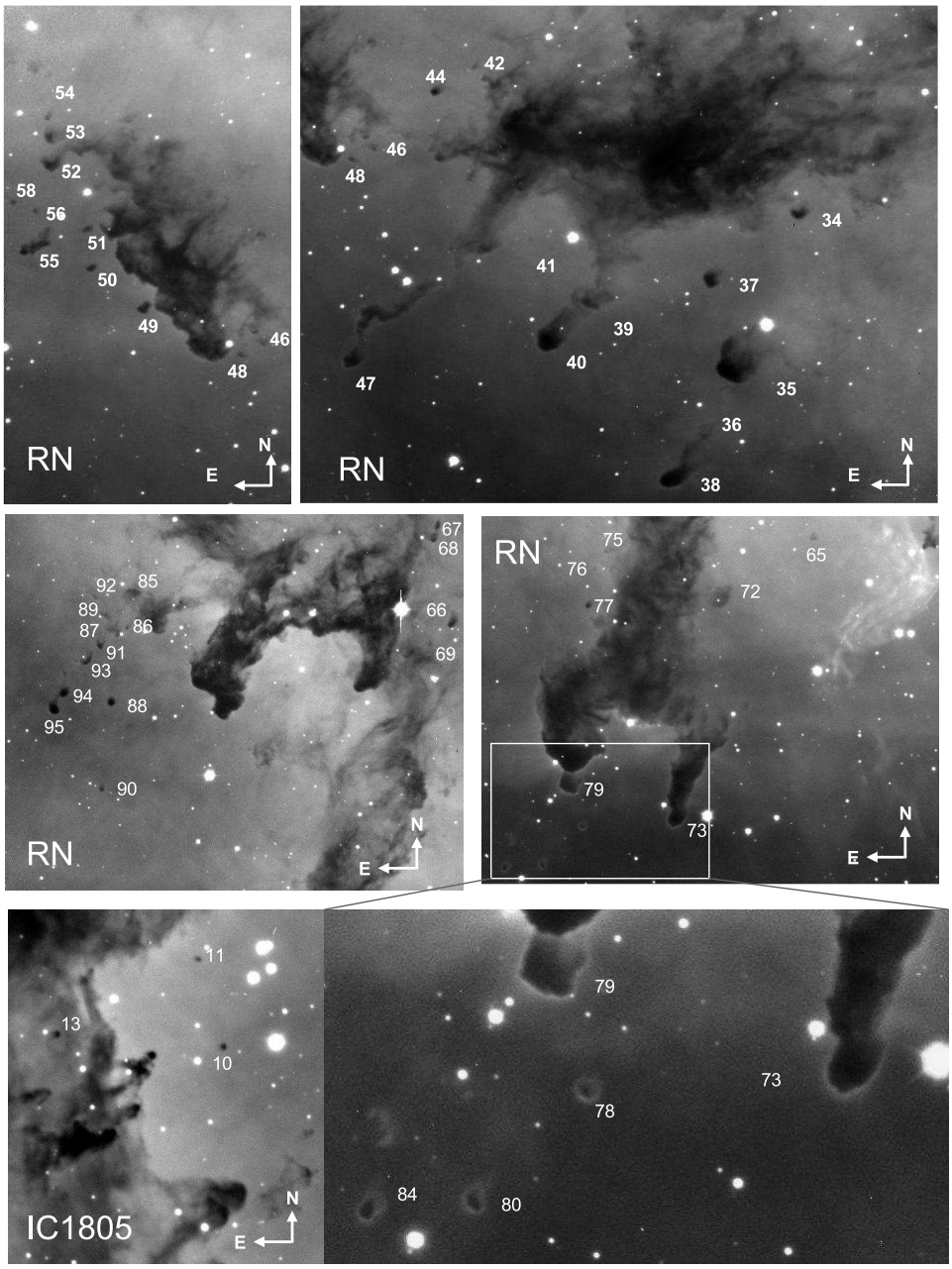

Figure 1: Globulettes in the Rosette Nebula (RN) and IC 1805. Hα narrowband images obtained at the Nordic Optical Telescope, La Palma, Spain. Reproduced from Gahm et al. (2007) with permission from the authors.

The first paper (Bertoldi, 1989) describes the radiation-driven implosion of a neutral spherical globule embedded in an ionized medium, assuming an initial top-hat function homogeneous density. The second paper (Bertoldi & McKee, 1990) describes an analytical model for cometary globules that have entered a state of pressure equilibrium between the ionization front at the side facing the ionizing source and the supporting pressure from the neutral gas in the cloud. Thermally as well as magnetically supported clouds were considered.

Numerical studies of the problem include Lefloch & Lazareff (1994), who performed 2-dimensional simulations of globules using a three-temperature equation of state, also investigating the transient phase before the equilibrium state numerically. Criteria for the stability of ionization fronts during the equilibrium cometary state were formulated, predicting that only clouds that form an inter-boundary layer of recombining gas downstream of the ionization front, consuming the majority of the ionizing photons, are stable against fragmentation during the equilibrium state. In Mellema et al. (1998) an approximate analytic model for photo-evaporating clumps was derived and tested against 2-dimensional numerical simulations, with good agreement; although originally derived for planetary nebulae conditions, the model is valid for a large range of photo-evaporating neutral clumps where the ionizing radiation can be approximated as plane parallel. Recent papers include Esquivel & Raga (2007), who studied the fragmentation of photo-evaporating clumps numerically in 3 dimensions, using a two-temperature equation of state, a heterogeneous initial density distribution and a divergent radiation field. Gravitational interaction was included and found to play a secondary role in photo-evaporating globules unless high compression is achieved during the initial implosion. Cerqueira et al. (2006) studied the behavior of the cometary tails of globules when exposed to radiation from two stars, a problem relevant in H II regions if the angular size of the central cluster relative to the globule is non-negligible.

The aim of this thesis is to establish a time scale for the photo-evaporation of globulettes in the Rosette nebula by matching observations and earlier analytical work to numerical simulations. Also, the possibility of gravitational collapse, leading to the formation of low-mass stellar objects, is addressed in an approximate way.

The theory section reviews analytical solutions of the problem, as formulated by Bertoldi (1989), Bertoldi & McKee (1990) and Mellema et al. (1998), using the assumption of a thermally dominated internal cloud pressure. Analytical estimates for the cloud lifetimes are derived. Approximate criteria for the onset of gravitational collapse are also obtained.

The hydrodynamical code used, CAPREOLE, and the initial setup of the simulated cases is described in the section on the numerical model.

Results from initial analytical considerations and the simulations are presented in the results section. Initial studies of the thermal model using

2-dimensional simulations are followed by a presentation of the results from 3-dimensional simulations. Numerically obtained values of the lifetimes are presented.

In the section on comparisons to observations, synthesized Hα images and lightcurves of simulated cases are presented. An approximate estimate of the observability of bright cloud rims is made.

The discussion section compares the derived lifetimes of globulettes to earlier work and addresses the possibility of the formation of planetary sized objects in globulettes.

2 Theory

2.1 Ionization fronts

The textbook description of an ionization front (IF) is that of a plane parallel front moving into a stationary homogeneous cloud of atomic hydrogen. The flux of matter across an ionization front is proportional to the flux of ionizing (> 13.6 eV) UV photons. Assuming every UV photon that reaches the neutral gas ionizes one hydrogen atom, the basic relation between the effective ionizing flux F_i and the speed of the shock front u relative to the medium being ionized is

$$u = \frac{F_i}{n} = \frac{F_i m}{\rho} \tag{1}$$

where n and ρ are the number and mass densities, respectively, and m the average mass per atom.

In the frame of the ionization front, due to the conservation of mass and momentum,

$$\rho_1 v_1 = \rho_2 v_2 \tag{2}$$

and

$$\rho_1 {v_1}^2 + p_1 = \rho_2 {v_2}^2 + p_2 \tag{3}$$

have to hold across the front, where indices 1 and 2 follow the usual convention of upstream and downstream, respectively, v is the velocity of the gas relative to the IF and p the gas pressure. Solving for the IF speed in terms of the isothermal sound speed $c = \sqrt{p/\rho}$, $u = |v_1| < u_D$ (D-type, dense IF solution) or $u = |v_1| > u_R$ (R-type, rarefied IF solution), where

$$u_D \approx \frac{{c_1}^2}{2c_2} \tag{4}$$

and

$$u_R \approx 2c_2, \tag{5}$$

if $c_2 \gg c_1$. The only allowed stable solutions at an ionization front must fall in one of these regimes. If $u_D < u < u_R$ (M-type IF), a shock will be

driven into the cloud, leading to a pileup of neutral, shocked gas upstream of the ionization front, such that the front eventually becomes D-critical and $u = u_D$.

2.2 Photo-evaporation of neutral clumps

The most detailed analytical description of the problem of a photo-evaporating neutral clump can be found in Bertoldi (1989) and Bertoldi & McKee (1990), who describe the characteristic stages of evolution and defines characterizing parameters for photo-evaporating knots. They also provide analytical and/or numerical calculations of some derived quantities for a wide range of characterizing parameters.

Initially, we consider a spherical neutral cloud with characteristic nuclei number density n_0 and radius r_0, which is exposed to an ionizing flux F. An ionization front will form on the side of the cloud facing the incoming UV flux. The heating at the exposed side will cause the ionized gas to expand into the environment while also driving a shock into the cloud perpendicular to the surface. Once the photo-evaporation flow of ionized gas is established, the gas in the flow will start recombining spontaneously, emitting in characteristic lines. This recombination provides a source of neutral matter which is re-ionized in the flow by the incident UV photons, effectively shielding off some of the radiation before it reaches the ionization front. The dimensionless maximum initial column density parameter

$$\eta = \frac{\alpha_i r_0 n_0}{c_2} \tag{6}$$

relates the column density, through the center of the cloud, to the equilibrium state of the shielding layer of recombining material downstream of the front, where the downstream isothermal sound speed is c_2 and recombination rate coefficient is α_i. In cases where $\eta < 1$, the equilibrium between ionization and recombination is not reached before the cloud is completely ionized. The shock velocity parameter ν relates the initial shock velocity $v_{s,0}$ to the downstream sound speed c_2 and is determined by the effective incident ionizing flux $F_i \leq F$ through

$$\nu = \frac{v_{s,0}}{c_2} = \sqrt{\frac{2F_i}{n_0 c_2}} \tag{7}$$

when conditions at the ionization front are M-type or D-critical. However, the equilibrium shock velocity is limited to c_2 as this is the expansion speed of the ionized matter; if $\nu > 1$ a weak R-type ionization front will initially move into the cloud. Due to the buildup of matter downstream of the ionization front the shielding layer will then become denser, lowering F_i and v_s, until the equilibrium state $v_s = c_2$ is reached. Conditions at the IF are

then M-type and a shock front is driven into the cloud. The equilibrium v_s is given by

$$v_s = \frac{\nu c_2}{\sqrt{\phi_D q}} \tag{8}$$

where

$$q \equiv \frac{F}{u n_0} = \frac{F}{F_i} \tag{9}$$

is the ratio between the incident ionizing flux and the flux of material across the ionization front and ϕ_D a factor of order unity, determined by the ionization balance at the front.

The photo-evaporation parameter ψ is a measure of the relative importance of recombination downstream of the ionization front. Bertoldi (1989) defines

$$\psi = \frac{\alpha_i F_i r_0}{{c_2}^2} = \frac{\nu^2 \eta}{2} \tag{10}$$

which is the average number of recombinations for a hypothetical hydrogen nucleus traveling a distance equal to r_0 in the evaporation flow, which has a characteristic expansion velocity equal to c_2. A large value (> 10) of ψ means that a nucleus will typically recombine and be re-ionized several times while in the evaporative flow, thus shielding the cloud and reducing the effective flux F_i that reaches the front; a low value means that recombination is insignificant and $F_i \approx F$.

There are two main phases of the photo-evaporation process; the initial implosion, or collapse phase, and the subsequent cometary phase. The implosion phase is characterized by the formation of an ionization front which is preceded by a shock moving into the cloud. Once the shock has moved through the entire cloud, the implosion phase is over and the cloud expands before entering an equilibrium cometary state. In this cometary state, a pressure gradient is maintained by the constant heating at the ionization front, causing the cloud to accelerate by a rocket effect as matter is ejected in the evaporation flow.

2.3 Mass evolution and lifetime estimates

Bertoldi (1989) points out that any large inhomogeneities in the initial cloud density distribution will tend to fragment the cloud, as the formation of local ionization fronts around local density peaks will tend to focus mass onto them. Conceptually, this is a form of Rayleigh-Taylor instability; more massive density knots will tend to be accelerated at a slower rate. This will aid fragmentation and eventually cause a scattering of fragment velocities. The total evaporation time will then be governed by the largest fragments.

Initially, the timescale and mass loss rate during the implosion phase is determined by the speed v_s of the shock moving into the cloud, such that

the characteristic shock crossing time at the center is

$$t_{sc} = 2r_0/v_s. \tag{11}$$

For clouds where the initial conditions are R-type (and v_s is c_2 limited), $t_{sc} = 2r_0/c_2$; otherwise,

$$t_{sc} = \frac{2r_0(q\phi_D)^{1/2}}{\nu c_2}. \tag{12}$$

During this phase, the cloud loses mass rapidly at a rate of

$$\frac{dM}{dt} = -F_i m A \tag{13}$$

where m is the average mass per nucleus and $A \propto M^{2/3}$ is the total area exposed to the flux. Using this approximation (Mellema et al. 1998) for the effective cloud area,

$$\frac{M(t = t_{sc})}{M_0} \approx 1 - \frac{F_i}{n_0 v_s} \tag{14}$$

and

$$\frac{M(t)}{M_0} = \left(1 - \left[1 - \left(\frac{M(t = t_{sc})}{M_0}\right)^{1/3}\right] \frac{t}{t_{sc}}\right)^3. \tag{15}$$

Alternatively, Bertoldi (1989) calculates

$$\frac{M(t = t_{sc})}{M_0} \approx \frac{v_s}{2c_2} \tag{16}$$

for $\psi \gg 10$, i.e. when shielding due to recombination is significant.

At the end of the collapse phase, the cloud has likely reached its highest compression, forming an elongated structure along the symmetry axis as the phase velocity of the ionization front will be faster further from the symmetry axis. If the ionization front is initially R-type and later c_2 limited, it will tend to collapse in a more spherical manner, leading to higher compression in the center of the sphere. Subsequently, the cloud will expand due to the overpressure on the shielded side of the cloud and eventually settle in the equilibrium cometary state. This happens on the timescale of a sound crossing time.

The equilibrium cometary state is characterized by hydrostatic equilibrium,

$$\frac{dp}{dx} = -a\rho, \tag{17}$$

with a constant high pressure being maintained at the ionization front. The cloud is accelerated at a rate a and has a characteristic scale height of

$$h = \frac{{c_1}^2}{a}. \tag{18}$$

Assuming D-critical conditions, the pressure of the neutral gas upstream of the front is (Mellema et al. 1998)

$$p \approx 2\rho u_1 c_2 \approx 2F_i c_2 m \cos\alpha \tag{19}$$

where α is the relative angle between the surface normal and the photon path in the approximately planar radiation field. At the peak, $p_c \approx 2F_i c_2 m$. It can be shown that the radius r of the cloud in cylindrical coordinates (r,θ, x) approximately obeys

$$r = h \arctan\left(\sqrt{e^{2x/h} - 1}\right), \tag{20}$$

which then can be used to estimate the total cloud mass and the accelerating force on the cloud. The scale height relates to the total cloud mass as

$$M = \left(1 - \frac{2}{\pi}\right) \pi^2 \frac{p_c}{{c_1}^2} h^3. \tag{21}$$

At any given time, the mass loss rate is

$$\frac{dM}{dt} = -F_i m \pi \left(\frac{\pi}{2} h\right)^2. \tag{22}$$

Mellema et al. (1998) go on to define the dimensionless variables $\tilde{t} = t/t^*$, $\tilde{h} = h/h_0$, where

$$t^* = \frac{24}{\pi}\left(1 - \frac{2}{\pi}\right)\frac{c_2 h_0}{{c_1}^2}. \tag{23}$$

In these variables, using an approximate expression for the flux reduction factor q, it is possible to solve for $M(t)$:

$$M(t) = M(t_{sc}) \left(\frac{1 + \eta_m}{1 + \eta_m \tilde{h}}\right)^{1/2} \tilde{h}^3 \tag{24}$$

where

$$\eta_m = \frac{\alpha_i F h_0}{3{c_2}^2}, \tag{25}$$

$$q = \frac{F}{F_i} \approx \sqrt{1 + \eta_m} \tag{26}$$

the scale height evolves with time approximately according to

$$\tilde{h} \approx \frac{\tilde{t}_m - \tilde{t}}{\tilde{t}_m - \tilde{t}_{sc}}, \tag{27}$$

and the characteristic evaporation time (including the initial collapse) for the cloud is

$$\tilde{t}_m = \tilde{t}_{sc} + \frac{5}{6} + \frac{1}{6\eta_m} \ln(1 + \eta_m). \tag{28}$$

The transient expansion phase is not included in this estimate as it is significantly shorter than the cometary phase, according to Bertoldi & McKee (1990), who also derive an analytical estimate of the characteristic evaporation time;

$$t_{ev} = 4.48 {c_1}^{-6/5} \phi_1 {S_{49}}^{-1/5} R_1^{2/5} \left(\frac{M_1}{M_\odot} \right)^{2/5} \text{ yrs}, \tag{29}$$

where the thermal evaporation time factor $\phi_1 \approx 1$, S_{49} is the source emission rate of ionizing photons in units of 10^{49} photons s^{-1}, R_1 and M_1 are the distance to the source and cloud mass at the beginning of the cometary phase. This assumes that the cloud is mainly supported by thermal pressure, and that the cloud has already acquired a typical velocity of ~ 5 km/s during the implosion phase.

2.4 Gravitational instability

The usual expression for the Jeans mass is

$$M_{Jeans} = C \frac{{c_1}^3}{G^{3/2} \rho^{1/2}} \tag{30}$$

where C is a factor on the order of unity. However, due to the pressure increase at the ionization front, there is a significant external pressure contribution at the ionization front, prompting us to use the Bonnor-Ebert mass

$$M_{BE} = 1.18 \frac{{c_1}^4}{G^{3/2} {p_{ext}}^{1/2}} \tag{31}$$

(Bertoldi & McKee, 1990) which, while omitting supporting pressure other than thermal (in particular, magnetic pressure), yields a lower limit to the external pressure p_{ext} required for collapse given a certain cloud mass. For photo-ionization to trigger gravitational collapse, $M_{BE} > M$.

The most likely time for a gravitational instability to form is at the end of the cloud collapse phase, when a significant portion of the cloud mass still remains while having been compressed to a fraction of the original size. However, when the cloud is gravitationally unstable, there must still be enough time available for the collapse to take place; that is, the free fall time

$$t_{ff} = \sqrt{\frac{3\pi}{32 G \rho}} \tag{32}$$

must be significantly shorter than the time spent in the critical state.

3 Numerical Model

3.1 Hydrodynamical code

The code used to numerically simulate the photo-evaporation process is called CAPREOLE (v. 3). It uses the Roe-Eulderink-Mellema solver which is a FORTRAN 90 implemented approximate Riemann solver, and the C2-Ray method (Mellema et al., 2006) for photon conservative ray-tracing. The code is parallelized with the MPI library, making it very scalable.

CAPREOLE solves the Euler equations on an equidistant grid of 1-3 dimensions. The gas is numerically represented by the state variables ρ (density), $\rho\mathbf{v}$ (momentum density), e (energy density) and χ_i (ionization fraction). Other state variables such as p and T are calculated as needed. The chemical abundances in the gas are treated approximately using fixed relative abundances, and an average mass per nucleus $m = \rho/n = 1.3$ corresponding to a standard He number density fraction of 0.1.

The code does not include self gravity, which can be justified provided that the escape velocity at the cloud surface $v_e \ll c_1$. This holds if the typical objects to be studied are Jeans unstable only by a very large contribution from external pressure. However, this also means that results, when conditions for gravitational instability are approached, are to be interpreted with some caution as the cloud, unphysically, will not be gravitationally contained.

3.2 Thermal model and photo-ionization

The dominant source of heating in the thermal model is the photo-ionization at the ionization front, which drives a shock into the neutral cloud. A plane parallel approximation of the photon flux was used in the ray tracing module. The flux of ionizing photons and energy contribution was calculated assuming a black-body spectrum with T_{eff} set to the mean black-body temperature from the ionizing stars. A mean value of $T_{eff} = 4.8 \times 10^4$ K for NGC 2244, the central cluster of the Rosette nebula, was adapted using values from Vacca et al. (1996), with a total photon emission rate $S = 1.44 \times 10^{50}$ s^{-1} (Cox et al., 1990). A global heating rate of $\Gamma = n_e \times 2 \times 10^{-16}$ cm^{-3}s^{-1} (Stahler & Palla, 2004) was also assumed, approximating heating from cosmic rays. Ambient emission from the H II region and penetrating < 13.6 eV UV photons have been excluded from the model, assuming the ionization heating to be the dominant source of energy input at the cloud rim.

The cooling function includes H recombination and collisional excitation. After the initial temperature model testing, this proved insufficient to reproduce the low temperatures commonly observed in globules. For the simulated cases presented, additional cooling at $T < 8000$ K was used and tuned to obtain equilibrium values in the observed range. In practice this

was implemented through the coronal cooling curve presented in Dalgarno & McCray (1972), which is dominated by collisional excitation of C II and Fe II at these temperatures. The value obtained from the cooling curve was multiplied by a cooling fudge parameter f_{cool}, which was tuned to obtain equilibrium temperatures in the 20 K range.

The summed contribution from heating and cooling is implemented as a source term in the energy equation. This source term is introduced in the solver through operator splitting.

3.3 2D simulations

Under the assumptions that the initial density knot is homogeneous and approximately spherical and that the ionizing radiation can be treated as plane parallel, a cylindrically symmetric simplification of the problem is justified. This greatly reduces the computational size of the problem at the expense of introducing geometrical source terms in the equation solver, due to the cell volume element

$$dV = 2\pi r dr dz \tag{33}$$

being r dependent. Across the symmetry axis ($r = 0$) there is no flux by definition as the innermost cells are cylinders, conceptually, without any inner border. The main disadvantage of the 2-dimensional representation is the inability to treat deviations from the symmetric case, as every cell represents a toroid in 3D space.

3.3.1 Initial conditions

The initial setup used for the 2D grid was a semicircular area of high, constant density, sitting on the $r = 0$ axis. This corresponds to a homogeneous sphere in cylindrical symmetry. Due to the absence of self-gravity in the code, as well as the tendency of any thin outer layer of the cloud to evaporate on a much shorter timescale than the denser parts of the cloud, a homogeneous density distribution was used to approximate the initial state of a globule embedded in a newly ionized medium. The environment was set up to have a lower, constant density. All of the simulated domain is assumed to start out at rest relative to the star. Within the first few time-steps of the simulation, the environment around the cloud will become completely ionized when an R-type ionization front moves through the simulation domain, much faster than the typical isothermal speed of sound ($c_0 \approx 0.3$ km/s) in the neutral gas. In order to have the cloud start out in approximate pressure equilibrium with its environment, the internal/external density ratio was chosen according to $\rho_0/\rho_{ext} \propto T_{ext}/T_0$, where $T_{ext} = 5.8 \times 10^3$ K is the typical observed temperature of the ionized environment (Celnik, 1985). This ensures that $p_0 \approx p_{ext}$ holds after the ionization front passes.

The uppermost frame of Figure 4 shows the initial simulation state. For this simulation run, an initial density and temperature for the cloud of $\rho_0 = 2.6 \times 10^{-20}$ and $T_0 = 18$ K, respectively, was used, with a photon flux of $F = 3.3 \times 10^{10}$ cm^{-2} s^{-1}, equivalent to a distance of 6 pc from the NGC 2244 central cluster. The initial cloud radius is 1.2×10^{17} cm, or 3.9×10^{-2} pc.

3.4 3D simulations

3.4.1 Initial conditions

In analogue to the 2D case, the basic setup of the 3D runs is a sphere of high density surrounded by a lower density medium.

The 3D code was initially set up to start out with an entirely symmetrical density distribution, similar to the 2D case. Early testing revealed, however, that in the absence of natural small fluctuations in the initial density distribution, the fragmentation process in the cloud is dominated by numerical effects, leading to unphysical symmetric patterns. Therefore, a randomly generated density fluctuation field was applied to the initial density distribution. The density field has the form

$$F(n) = \sum_{n=n_{min}}^{n_{max}} 2\pi n a_n P(n)^{1/2} e^{i(2\pi n \mathbf{r} + \phi)} \tag{34}$$

in Fourier space, where $n = L/\lambda$ is the wavenumber of the density fluctuation, a_n is a randomly generated gaussian variable using mean 1 and standard deviation 1, multiplied by a random phase factor $e^{i\phi}$, and $P(n) \propto n^m$ is the weighting function using a spectral index of $m = -11/3$ (Esquivel et al. 2003, Esquivel & Raga 2007). Using the inverse discrete Fast Fourier Transform (IFFT) a random density field $f(\mathbf{r}) = \mathrm{IFFT}(F(n))$ was generated in $\mathbf{r}$ space. In order to maintain an equal resolution along the spatial axes, a cubic density distribution field was generated and subsequently rescaled and cut to fit the size of the computational grid. The density fluctuation field $f(r)$ was then normalized to $\langle f \rangle = 1$ and $\sigma_f = 0.1$. The initial state of the density distribution can be expressed as

$$\rho(\mathbf{r}) = \begin{cases} f(\mathbf{r})\rho_0 & |\mathbf{r}| \leq r_0 \\ f(\mathbf{r})\rho_{ext} & |\mathbf{r}| > r_0 \end{cases} \tag{35}$$

if we take $\mathbf{r} = \{0, 0, 0\}$ to be the cloud center. The high/low density border at r_0 was smoothed linearly with a 5 pixel wide transition region to avoid initial numerical difficulties. The effective wavelength cutoffs for the power law weighting function, in the final distribution, are r_0 for the largest size fluctuations and 6 cells for the smallest fluctuations, corresponding to 6.4×10^{15} cm in the standard size simulation. Below the 6 cell threshold the

Model	r_0 [10^{16} cm]	n_0 [cm^{-3}]	T_0 [K]	M_0 [M_{Jup}]	R_0 [pc]
A	8.0	1.2×10^4	18	29.5	6
B	8.0	1.2×10^4	18	29.5	12
C	16.0	1.2×10^4	18	236	6

Table 1: 3D simulations. Initial state parameters.

density field was linearly interpolated in the rescaling. The setup allows for a slightly asymmetric mass distribution and deviations from the nominal initial cloud mass M_0, which assumes a homogeneous sphere as the initial state of the cloud; however, any random discrepancies are typically on the same order as numerical errors arising from discretization and smoothing, making them insignificant for the purposes of determining the cloud lifetime.

For the 3D simulations, three models were studied (Table 1):

- Case A, constituting the "standard" low mass globulette placed at a distance of 6 pc from the central cluster.
- Case B, which is case A placed at twice the distance (12 pc) from the central cluster. This represents a more extreme case, addressing the uncertainty in determining the true physical distance from observations, due to projection effects. The flux is effectively 25 % of the case A baseline value.
- Case C, which is the standard case with $2 \times r_0$ and $8 \times M_0$, putting the initial cloud mass in the low stellar range at 0.2 $M_\odot$.

In order to keep initial conditions consistent all three simulations were done on a $900 \times 150 \times 150$ equidistant Cartesian grid, using an identical random seed for the density fields and an identical initial density. Due to the rocket effect experienced by the cloud and the resulting > 10 km/s velocities acquired by remaining fragments over the course of the simulation, an elongated grid was necessary in order to capture the late evolution stages, limiting the possible grid resolution. The cloud center was placed at a distance of $2r_0$ from the $x = 0$ edge, which is enough to capture the shielding effects of recombination in the expanding photo-evaporation flow. The number of recombinations drops quickly with distance from the ionization front and the effective width of the recombination layer is about $0.1 - 0.2 \times r$ for a wide range of parameters (Bertoldi 1989).

4 Results

4.1 Initial analytical estimates

The analytical lifetime estimates from Mellema et al. (1998) and Bertoldi & McKee (1990) outlined in the theory section were applied to a number

of initial parameters similar to those observed in Rosette Nebula globules (Gahm et al. 2007). (Table 2, Figure 3). By applying the Bertoldi (1989) parameterization (Figure 2), it can be concluded that clouds observed in the Rosette Nebula generally fall in region II of the cloud parameter space, close to the $v_s = c_2$ border which divides region II from region III. Clouds in region II will form a stable ionization front with a shock moving at speed $v_s < c_2$ preceding the ionization front into the cloud. The lifetime estimates predict the lifetime of a spherical globule starting out at a given homogeneous density and radius at $t = 0$, right before the ionization front starts moving into the cloud. First, the initial implosion time is calculated as the cloud crossing time t_{sc} at the shock velocity, after which the cloud is assumed to have lost 1/2 of its initial mass. The lifetime of the cloud is then calculated using the post-implosion mass and effective flux, assuming the cloud settles into an equilibrium configuration as outlined in the theory section. It was noted that the equilibrium model predicts smaller sizes for the clouds given a certain initial mass than the typical cloud radii observed. In Figure 3 the analytical lifetime estimates are presented, along with the free-fall times that correspond to the homogeneous cloud densities in the estimate. From this estimate, it can be concluded that clouds in the lower globulette mass range ($\sim 10 M_{Jup}$) generally have free-fall times longer or of the same order as the expected lifetimes calculated from the initial mass, while the free-fall times of large clouds ($\sim 10^3 M_{Jup}$) are long enough to allow gravitational collapse, provided that an instability forms.

4.2 2D test results

Initial 2D testing showed the importance of the cooling function when studying the cloud compression. Observations of CO line emission in Rosette Nebula globules indicate globule temperatures in the 15-20 K range (González-Alfonso & Cernicharo, 1994), which implies that any heating from shocks and the ambient radiation field does not govern the overall measured properties of a typical cloud. After the initial temperature studies, the cloud temperatures in the simulation stabilized around 600 K, which is inconsistent with observed temperatures. Also, 600 K equilibrium temperatures would contradict the high dust absorption in globules. Dust cooling, while not part of the original temperature model, is likely to be an important process in the thermal model. To mimic this effect in an approximate way and obtain realistic equilibrium temperatures, extra coronal cooling was added as described in section 3.2. The cooling fudge f_{cool} parameter was adjusted to a value of 0.01 to provide sufficient cooling on a $t < t_{sc}$ timescale, making the shock preceding the ionization front effectively isothermal.

Numerical mass evolution studies revealed that the 2-dimensional simulations ran into resolution related problems. If the cloud can be assumed to cool fast enough to maintain its typical ~ 20 K temperature during the

r_0 [10^{16} cm]	n_0 [10^3 cm^{-3}]	M/M_{Jup}	t_{ff} [10^5 yrs]
2.2	69	3.7	3.2
3.7	28	6.9	5.0
5.9	18	18.9	6.1
∘ 8.0	12	29.5	4.5
12	18	94.5	7.8
15	11	185	7.8
37	6.9	1730	10

	Mellema et al.		Bertoldi			
M/M_{Jup}	t_0 [kyrs]	t_m [10^5 yrs]	t_{sc} [kyrs]	t_{ev} [10^5 yrs]	η	ν
3.7	2.2	2.1	3.4	1.3	352	0.92
6.9	2.4	2.6	4.1	1.6	234	1.5
18.9	3.5	3.8	6.0	2.4	250	1.8
∘ 29.5	3.9	7.6	7.0	2.8	218	2.3
94.5	6.3	7.1	11	4.6	312	2.2
185	8.5	9.2	15	6.0	390	2.3
1730	20	22	36	15	586	2.9

Table 2: Analytically estimated lifetimes for initial states similar to observed values for globulettes (Gahm et al. 2007). The case marked with ∘ is case A in the numerical simulations.

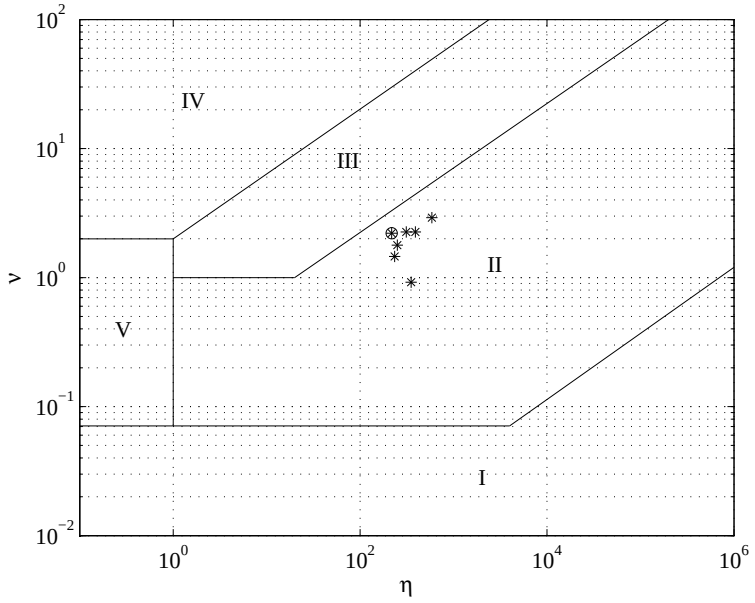

Figure 2: Photo-evaporating cloud parameters from table 2, following Bertoldi (1989), with η as the dimensionless column density and ν as the dimensionless initial shock velocity. All the considered cases fall into region II, which indicates that a shock will move into the cloud at a speed $v_s < c_2$. The case indicated with a circle is case A.

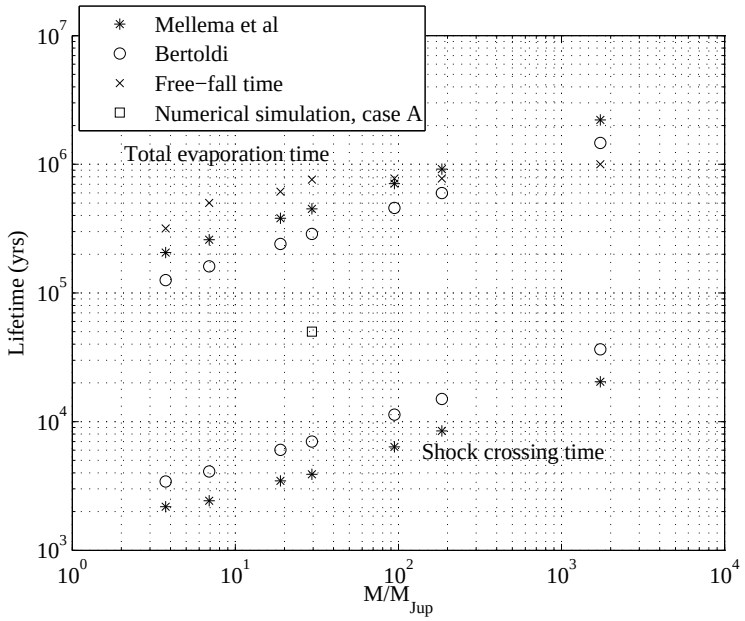

Figure 3: Analytical shock crossing and total life time estimates for the clouds considered in table 2. Free-fall time estimates are also included, indicating collapse times around 10^6 yrs.

collapse it will be compressed to a region only a few simulation cells wide at the very end of the collapse, before re-expanding into the equilibrium state. However, large mass fluxes in the r direction, first onto the symmetry axis and then away from it, will cause large source terms due to the geometrical effects in the equation solver. These contributions are on the same order as the flux terms when close to the symmetry axis. The conservative nature of the code was thus not maintained and the numerical global mass estimates were shown to be inconsistent with the physical situation.

Figure 4 shows the evolution of a 100 M_{Jup} 2D simulated case on a 1024×256 grid. Temperature profiles along the cloud symmetry axis for the times indicated are shown in Figure 5. Almost instantly, the rarefied medium around the cloud is ionized by an R-type shock, except where the cloud is shielding the neutral gas. The low pressure due to the absence of heating here causes a flow of ionized gas into the shadow, where it cools. This creates a denser region in the shadow of the cloud, stretching into infinity due to the plane parallel approximation of the radiation field. The amount of neutral matter in the part of the shadow that was included on the grid, however, was found to be insignificant in comparison to the amount of original cloud material. In reality, the amount of material in the shadow of the cloud is likely even smaller, since the effective angular size of the

NGC 2244 central cluster at a distance of $R = 6$ pc is likely large enough to limit the size of the shielded region to $< 10\ r$, with r as the projected radius of the shielding ionization front. For a detailed study on the effects on clouds exposed to several ionizing sources, see Cerqueira et al. (2006).

During the initial implosion phase, the front moves through the cloud, preceded by a thin, highly compressed shocked layer. At 8 kyrs after the formation of the ionization front in the cloud, the shock has moved through the cloud while the large pressure at the front has compressed the cloud to a small structure moving along the symmetry axis. The exact size of the cloud at this point is dependent on the cloud temperature (Figure 5) and the supporting thermal pressure. Subsequently, the cloud re-expands into the equilibrium configuration, which it has reached by $t = 16$ kyrs, while being accelerated by the rocket effect caused by the evaporating material. In the final frame, at $t = 32$ kyrs, the shape of the cloud is beginning to deviate from the initial equilibrium configuration and a large portion of its mass is concentrated into a ring-like structure detached from the symmetry axis. This likely signifies the onset of fragmentation, although this process cannot be accurately represented in cylindrical symmetry. Based on this simulation, typical lifetimes were expected to fall in the $\sim 1 \times 10^5$ years range, although the previously mentioned global mass inconsistencies indicate that this is a very approximate estimate.

4.3 3D simulation results

On a Cartesian grid, the earlier mentioned global mass numerical problems, in the 2D cylindrically symmetric version, due to comparatively large source terms in the equations and large fluxes close to the symmetry axis, are avoided. The cloud is free to implode asymmetrically, which is important when using a random density field as the exact center of the density knot(s) might end up slightly off the nominal symmetry axis along the center of the grid.

For the cloud mass evolution studies this mass was defined as the total neutral mass in the simulated domain,

$$M = \sum \rho(1 - \chi_i)dV, \tag{36}$$

as the contribution to the total amount of neutral matter from non-original cloud matter, in the shadow region, is negligible compared to the neutral original cloud mass remaining. Additionally, the mass contained in the shadow is largely dependent on the presence of shielding high density knots. It will to first approximation be determined by, and proportional to, the effective shadowing area, thus not significantly altering the lifetime estimates. The photo-evaporation lifetime in the simulation t_l is here defined through $M(t_l) = 0.1\ M_0$, the time for the cloud to lose 90 % of its initial mass. Effectively, the distance moved by the cloud through the computational domain,

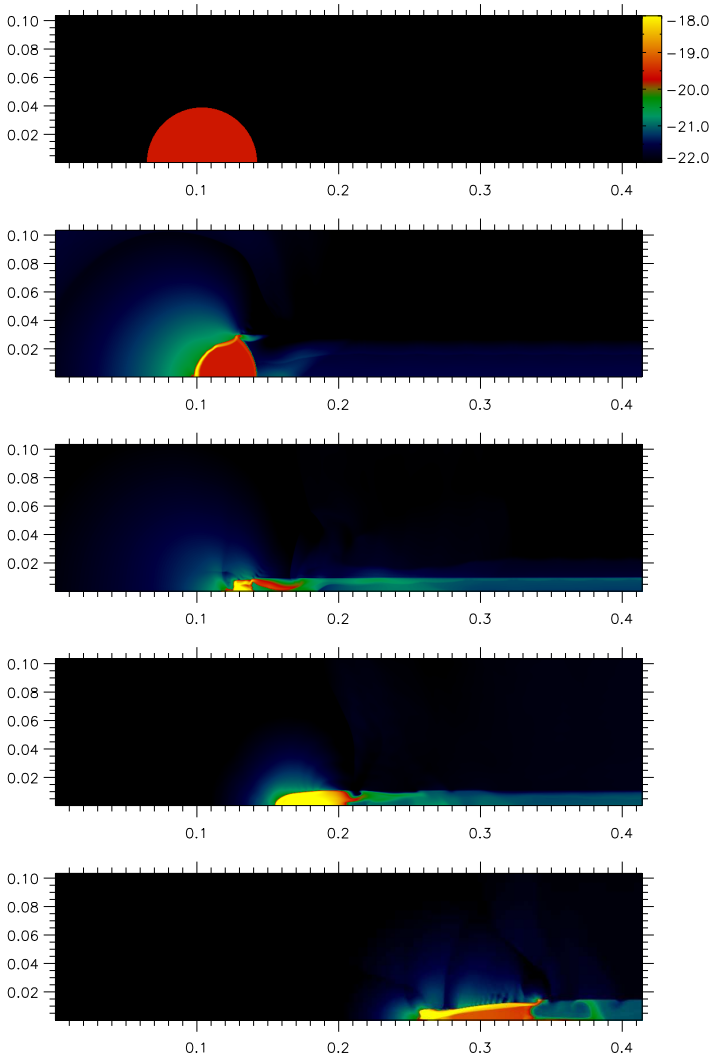

Figure 4: 2-dimensional simulation of a $M_0 = 100 M_{Jup}$ cloud at a distance of 6 pc from the central cluster of the Rosette nebula, at $t = 0$, 4, 8, 16 and 32 kyrs. Colors show $\log_{10} \rho$ in g cm^{-3}. Distances are in pc.

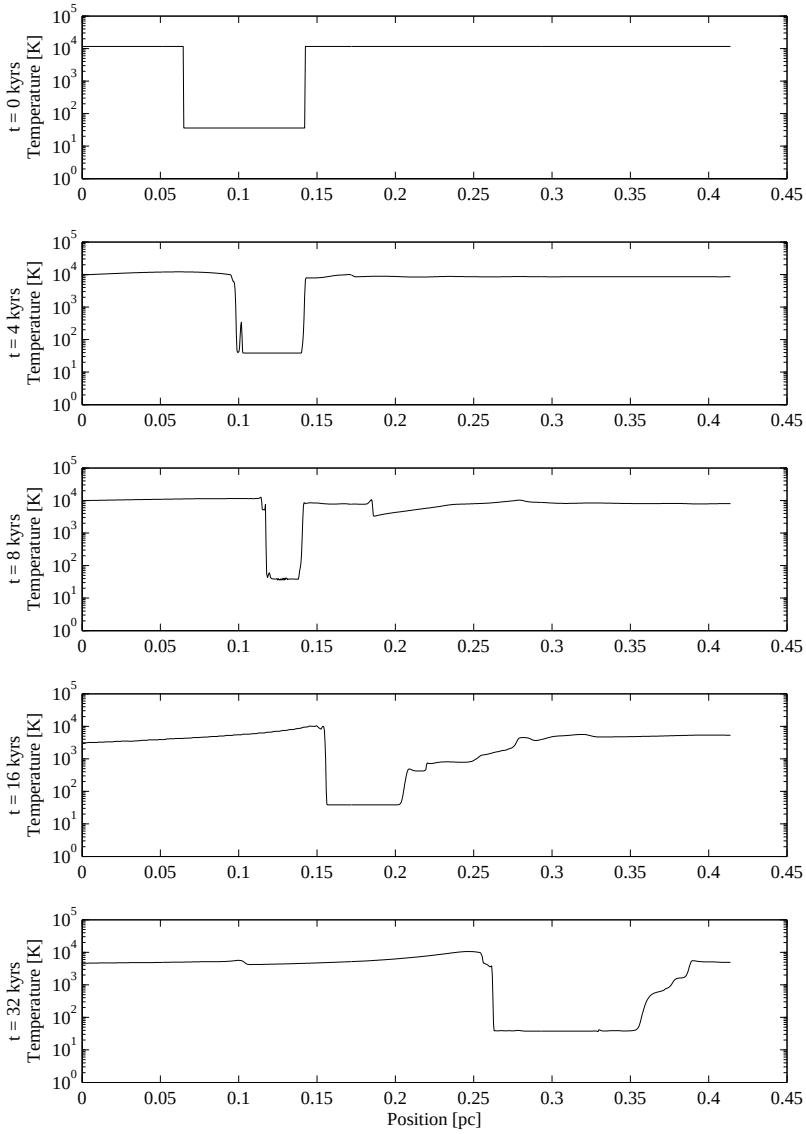

Figure 5: Temperature profile along the symmetry axis at $t = 0$, 4, 8, 16 and 32 kyrs, for the 2D simulation depicted in figure 4.

due to the rocket acceleration, along with numerical difficulties in dealing with high gradients, make studies of the very final evolution stages numerically expensive. There is also the potential for loss of accuracy due to poor resolution.

4.3.1 Case A, standard low-mass globulette

This case represents a standard low-mass globule in the Rosette nebula, set up to study the evolution of density knots comparable in size and density to observed globulettes. In Figure 6 the evolution of the cloud density is shown. The initial state is shown in the first frame, where also the 10 % density inhomogeneities are visible. By the second frame at $t = 2$ kyrs, the environment is ionized, except for the part situated in the cloud shadow. A thin highly compressed layer has developed inside the ionization front. At $t = 7$ kyrs, the implosion is complete, and due to the shape of the converging ionization front the cloud has formed a somewhat elongated, very dense ($\rho > 10^{-16}$) g cm^{-3} knot. The cloud is now moving at approximately the shock velocity, v_s, relative to the simulation frame (Figure 8). During the subsequent expansion, the cloud starts fragmenting due to to the uneven evaporation rate and acceleration experienced by different parts of the cloud, as determined by the density and morphology of the ionization front, which also affects the shielding from the recombinating layer. By 25 kyrs the cloud has several distinct high density knots that are only loosely attached. The plane of the density plot is somewhat adjusted between the last three frames to accommodate the fact that the largest fragments are not located in the central plane. In the final frame at 42 kyrs, the cloud is broken up into quickly evaporating pieces. From the mass evolution plot in Figure 7, a lifetime of $t_l \approx 5 \times 10^4$ yrs can be extrapolated. As seen in Figure 8, the cloud moves 0.3 pc over the duration of the simulation which is much lower than R, the distance to the central cluster. It is low enough to not affect the ionizing flux significantly. In cases where the cloud moves a distance comparable to R, lifetimes will increase correspondingly.

4.3.2 Case B, low-mass globulette at large distance

A cloud which is placed at a larger distance from the central cluster, lowering the UV photon flux F, can be expected to have a longer lifetime. From equation 29,

$$\frac{t_{ev,B}}{t_{ev,A}} \approx \left(\frac{R_{1,B}}{R_{1,A}} \right)^{2/5} \tag{37}$$

which for $R_{1,B} \approx 2 \times R_{1,A}$ implies a 30% longer lifetime as compared to the baseline case. From Figure 10, a lifetime $t_l = 7 \times 10^4$ yrs is established, which is consistent with the analytical estimate for the central cluster distance dependence. The acceleration rate of the cloud (Figure 11) is lowered due

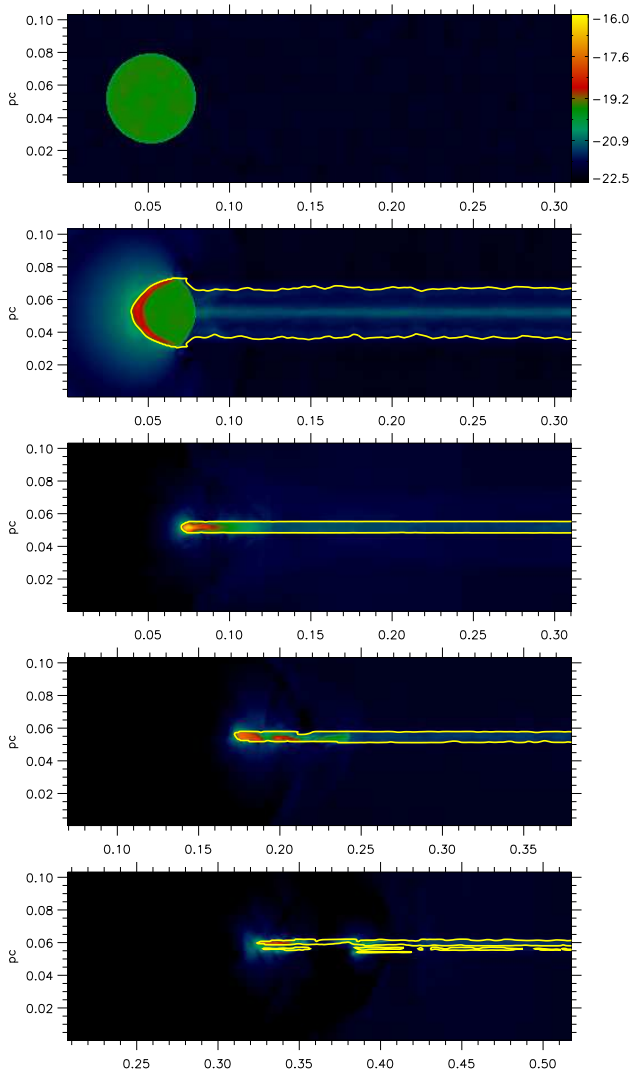

Figure 6: Case A. 3-dimensional simulation of a $M_0 = 29.5 M_{Jup}$ cloud at a distance of 6 pc from the central cluster of the Rosette nebula, at $t = 0$, 2, 7, 25 and 42 kyrs. Colors show $\log_{10} \rho$ in g cm^{-3} in a cut through the center of the cloud. The contour line indicates the transition between mainly neutral and mainly ionized gas at an ionization fraction $\chi_i = 0.5$. Distances are in pc. Only part of the grid is shown in the individual frames, as indicated by the length scale.

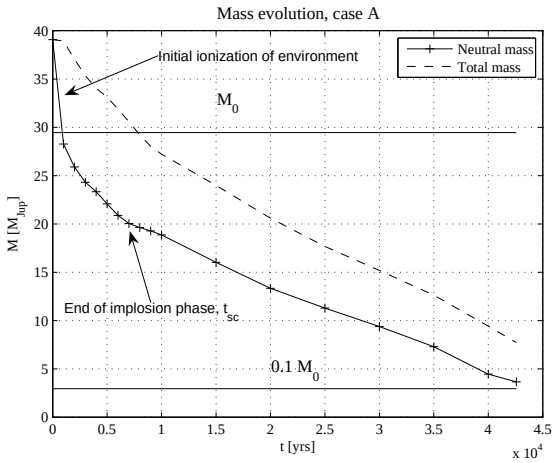

Figure 7: Mass evolution, case A. The upper curve is the total mass in the simulated domain and the lower curve shows the total amount of neutral matter. Horizontal lines show initially contained cloud mass M_0 and 0.1 M_0, in Jupiter masses.

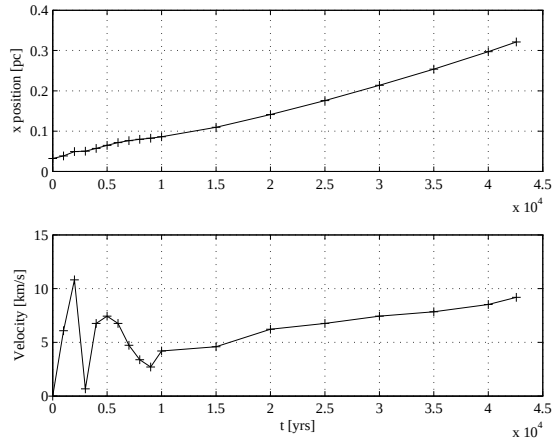

Figure 8: Position and velocity of highest density knot, case A. *Top*: Cloud core position x on the grid in pc, corresponding to the length scale in the simulation outputs, as a function of time. *Bottom*: Mean velocity $\Delta x/\Delta t$ of highest density knot in km/s.

to the lower peak pressure at the ionization front, but the cloud still reaches > 10 km/s velocities before evaporating completely. The fluctuations in calculated mean velocity are likely caused by the differentiated acceleration of the fragments and shifting relative densities of fragments, due to the cloud position $x(t)$ being defined as the highest density point at time t.

4.3.3 Case C, stellar-mass globule

By doubling the initial radius of the globule as compared to case A, we obtain a cloud with a mass in the low stellar mass range (0.2 $M_{\odot}$). From analytical considerations, we expect a power law mass dependence for equilibrium state clouds,

$$t_{ev} \propto M^{i} \tag{38}$$

with index $i = 2/5$ (Bertoldi) assuming a high ionizing flux with a photo-evaporation parameter $\psi > 10$. The same result is obtained from Mellema et al. (1998), with $\eta_m \gg 1$. For the initial implosion stage, assuming a homogeneous density, the shock crossing time is roughly proportional to the initial length scale with $t_{sc} \propto r$. A doubling of the cloud length dimensions yields a lifetime increase of about 2-2.3 times, depending on the amount of shielding from recombinations; $\psi > 10$ holds for all cases considered here. From the plot in Figure 13, the lifetime in the simulation is $t_l = 1.2 \times 10^5$ yrs, which is consistent with the power law assumption in the analytical estimate. Due to the longer survival time of the cloud relative to the standard mass cases, the distance moved by the cloud (Figure 14) is significantly larger and by the 90 % evaporation time t_l it has moved 1 pc.

4.4 Jeans instabilities and gravitational collapse

The criterion for Jeans instability (equation 30) means, for an internal sound speed of $c_1 = 3 \times 10^4$ cm/s, that the Jeans mass is about

$$1.57 \times 10^{24} C \rho^{-1/2} \text{ g} \tag{39}$$

and that the cloud needs to exceed this mass for a free-fall time. The highest local cell densities reached in the simulations is in the $\rho \approx 1 \times 10^{-16}$ range, which indicates a Jeans mass $\sim 100\ M_{Jup}$. It can be concluded that no sub-cell sized local instabilities will arise from the degree of compression alone, because with a cell spacing of 2.1×10^{15} cm the local mass contained in a single cell will then be about 0.5 M_{Jup}. For the standard mass (29.5 M_{Jup}) A and B cases, a collapse is unlikely as the cloud does not exceed its Jeans mass even at the point of highest compression. The Bonnor-Ebert mass (eq. 32) may be exceeded momentarily in the coldest parts of the cloud if the compressing pressure is taken as the highest pressure at the ionization front; however, this is likely an oversimplification with regard to the temperature

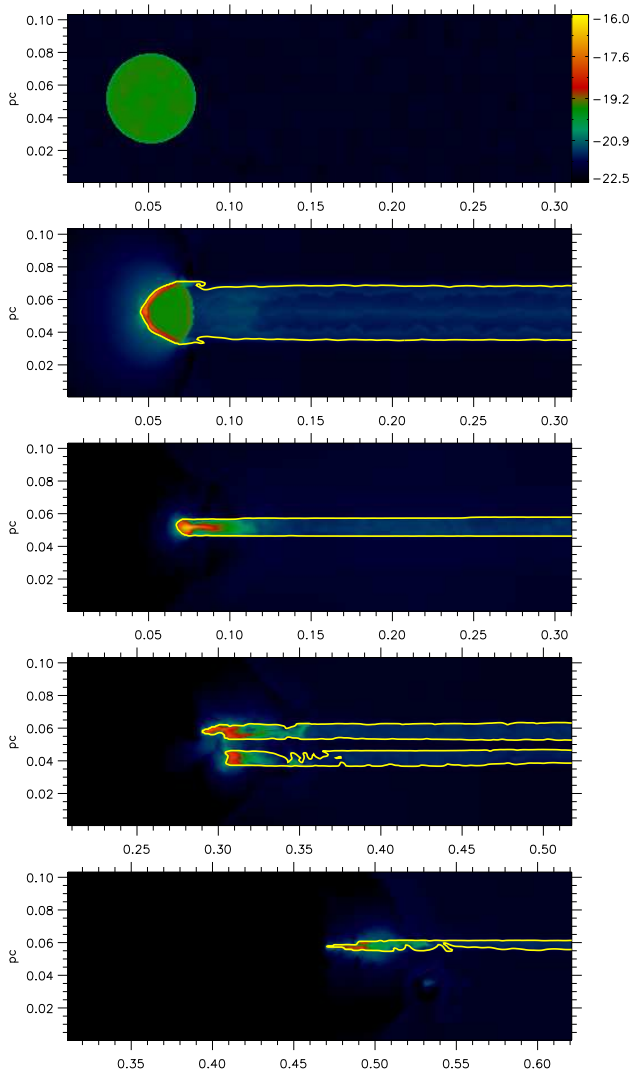

Figure 9: Case B. 3-dimensional simulation of the same $M_0 = 29.5 M_{Jup}$ cloud as in case A, at a distance of 12 pc from the central cluster of the Rosette nebula, at t = 0, 4, 10, 50 and 70 kyrs. Colors show $\log_{10} \rho$ in g cm^{-3} in a cut through the center of the cloud. The contour line indicates the transition between mainly neutral and mainly ionized gas at an ionization fraction $\chi_i = 0.5$. Distances are in pc. Only part of the grid is shown in the individual frames, as indicated by the length scale.

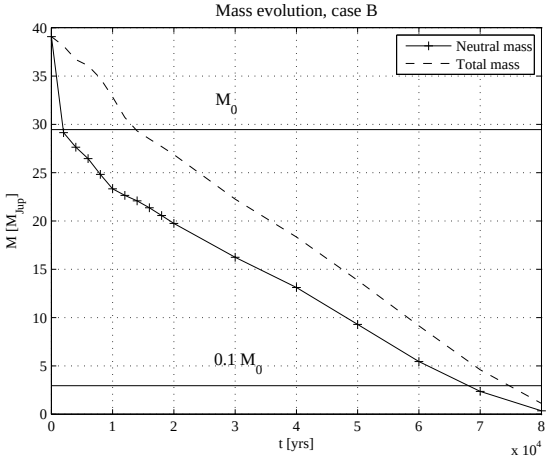

Figure 10: Mass evolution, case B. The upper curve is the total mass in the simulated domain and the lower curve shows the total amount of neutral matter. Horizontal lines show initially contained cloud mass M_0 and 0.1 M_0, in Jupiter masses.

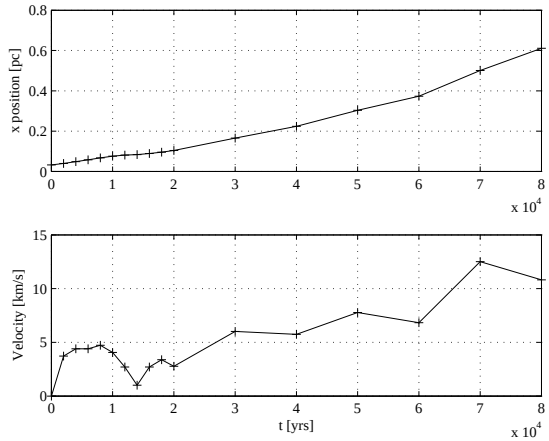

Figure 11: Position and velocity of highest density knot, case B. *Top*: Cloud core position x on the grid in pc, corresponding to the length scale in the simulation outputs, as a function of time. *Bottom*: Mean velocity $\Delta x/\Delta t$ of highest density knot in km/s.

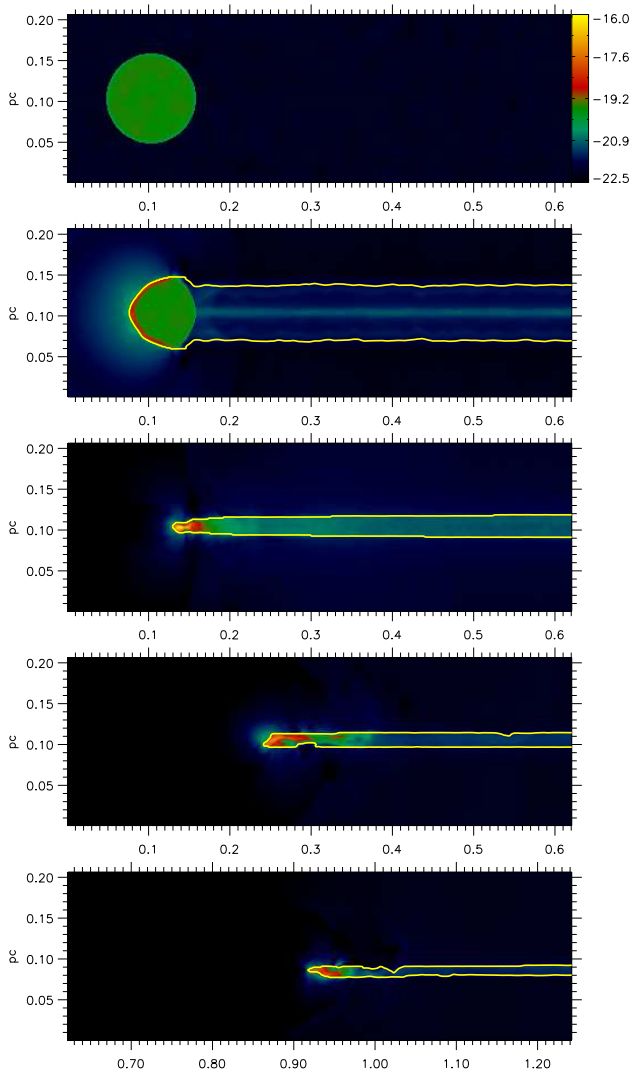

Figure 12: Case C. 3-dimensional simulation of a $M_0 = 236 M_{Jup} = 0.2 M_\odot$ cloud, at a distance of 6 pc from the central cluster of the Rosette nebula, at t = 0, 4, 14, 40 and 120 kyrs. Colors show $\log_{10} \rho$ in g cm^{-3} in a cut through the center of the cloud. The contour line indicates the transition between mainly neutral and mainly ionized gas at an ionization fraction $\chi_i = 0.5$. Distances are in pc. Only part of the grid is shown in the individual frames, as indicated by the length scale.

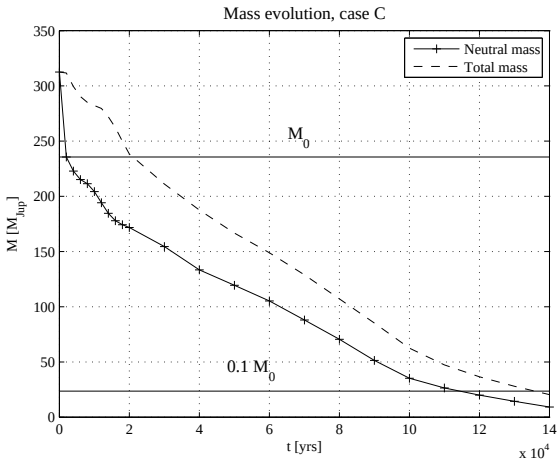

Figure 13: Mass evolution, case C. The upper curve is the total mass in the simulated domain and the lower curve shows the total amount of neutral matter. Horizontal lines show initially contained cloud mass M_0 and 0.1 M_0, in Jupiter masses.

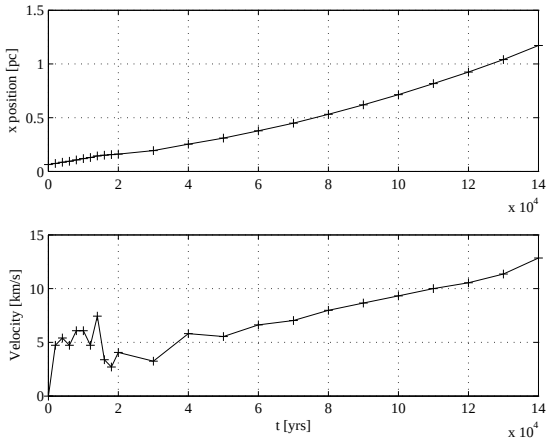

Figure 14: Position and velocity of highest density knot, case C. *Top*: Cloud position x on the grid in pc, corresponding to the length scale in the simulation outputs, as a function of time. *Bottom*: Mean velocity $\Delta x/\Delta t$ of highest density knot in km/s.

structure of the compressed density knot. The free-fall time associated with the highest densities reached is still around 6×10^3 yrs while the critical state only lasts for $< 10^3$ yrs in the simulation. For the 236 M_{Jup} case C, the cloud mass is approximately equal to the 100 M_{Jup} Jeans mass during the time of maximum compression. It must be concluded that for clouds in or above this mass range, gravitational effects can be significant. During the equilibrium cometary phase, there is no indication of Bonnor-Ebert type instabilities in any of the simulated cases.

5 Observational Comparisons

5.1 Lightcurves

An approximate estimate of the total emission from recombination lines in the cloud can be made using a volume integrated emission measure,

$$\int (n_{HII})^2 dV, \tag{40}$$

which is approximately proportional to the line emission from recombination lines. In order to correct for the background emission from the surrounding ionized gas, two integration volumes were chosen, one containing the cloud and one entirely outside the cloud, with the net cloud emission then estimated as the difference. The emission from the cloud during the initial collapse (Figure 15) drops by an order of magnitude during the initial implosion stage, during which the exposed cloud area is significantly reduced. After the globulette has reached the equilibrium state, the emission measure seems largely governed by the cloud cross section and proportional to the mass loss rate, as implied by the mass evolution (Figure 7).

5.2 Hα synthesized images

The tendency of the simulated clouds to fragment requires a synthetic imaging approach in order to better capture the sometimes complex cloud morphology. Synthesized Hα images at different viewing angles were created using an approximate radiative transfer equation

$$I_{H\alpha,n+1} = I_{H\alpha,n} e^{-\tau_d} + j_{H\alpha} \tag{41}$$

with the optical depth τ_d and emission $j_{H\alpha}$ calculated separately for every simulation cell. For the optical depth,

$$\tau_d = \sigma_d n_H \Delta s, \tag{42}$$

a standard dust extinction ratio per hydrogen atom of $\sigma_d = 5 \times 10^{-22}$ cm^2 / H is used. The emission coefficient $j_{H\alpha}$ was calculated using tabulated

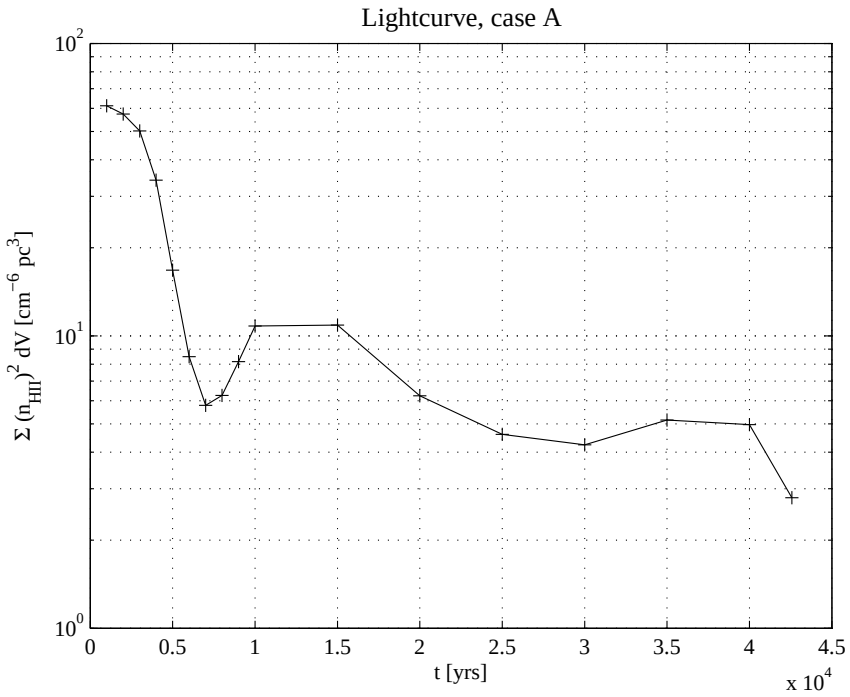

Figure 15: Lightcurve for simulated case A. The plot shows the volume integrated, background subtracted emission measure from the cloud, as defined by the integral $\int_{cloud}(n_{HII})^2 dV - \int_{bg}(n_{HII})^2 dV$, in $\mathrm{cm}^{-6}\mathrm{pc}^3$.

values for H recombination lines from Osterbrock (1989). With a distance of 1.4 kpc to the NGC 2244 cluster (Ogura & Ishida, 1981) flux estimates can be made for typical background emission levels as found in e.g. Celnik (1983). Here a background flux density $F_{bg} = 1 \times 10^{-15}$ ergs cm^{-2} s^{-1} arcsec^{-2} is assumed. Foreground emission and absorption outside of the simulation grid have generally been omitted.

Figure 16 displays the cloud as seen from different angles. From these images it is evident that a fragmented or fragmenting cloud can appear very different morphologically, depending on the viewing angle. Comparing to observed globulettes (Figures 17, 18), the morphological similarity to large globulettes is evident, although clouds comparable in size to the smaller simulated cases are close to the lower observational size limit, making it difficult to resolve small structure. In the synthesized images, the emitted flux along the bright cloud rim is $< 5\%$ of the background levels typical for the brighter regions in the Rosette Nebula. Consequently, in bright regions, the background emission is likely to be too high for bright rims to be observable. However, in regions with a significantly lower Hα background flux than the assumed 1×10^{-15} ergs cm^{-2} s^{-1} arcsec^{-2}, globulettes similar to the simulated standard case should have visible bright rims. One pixel in the image equals 0.10 arcsec; for earth-based observations, seeing effects need to be accounted for as well.

6 Discussion

6.1 Discussion

The lifetimes indicated by the numerical simulations, $t_l \approx 5 \times 10^4$ yrs, are significantly shorter than expected from analytical considerations (Figure 3), by a factor $\sim 5 - 10$. The mass loss rate of the cloud is proportional to the area exposed to the ionizing flux. Therefore, the most likely reason for a higher than expected mass loss rate is that the exposed cross section of the cloud is not accurately described by the analytical solution for the equilibrium cometary cloud. For a fragmented cloud, this is the case; by assuming $A_0 \propto M^{2/3}$, it is quickly realized that N clouds, each with mass M/N have a combined area $\propto N \times (M/N)^{2/3} = MN^{1/3}$. The resolution of the simulation will tend to set a lower limit for the exposed area of unresolved density knots, possibly leading to a quicker evaporation time in the simulation for very small fragments. The cloud fragmentation and smaller characteristic radius of the ionization fronts will also tend to cause more divergent evaporation flows, reducing the recombination shielding factor q. By the definition of q this is equivalent to an increased photo-evaporation flow given a certain ionizing flux.

Reipurth et al. (2003), in their study of Thackeray's globules, estimate

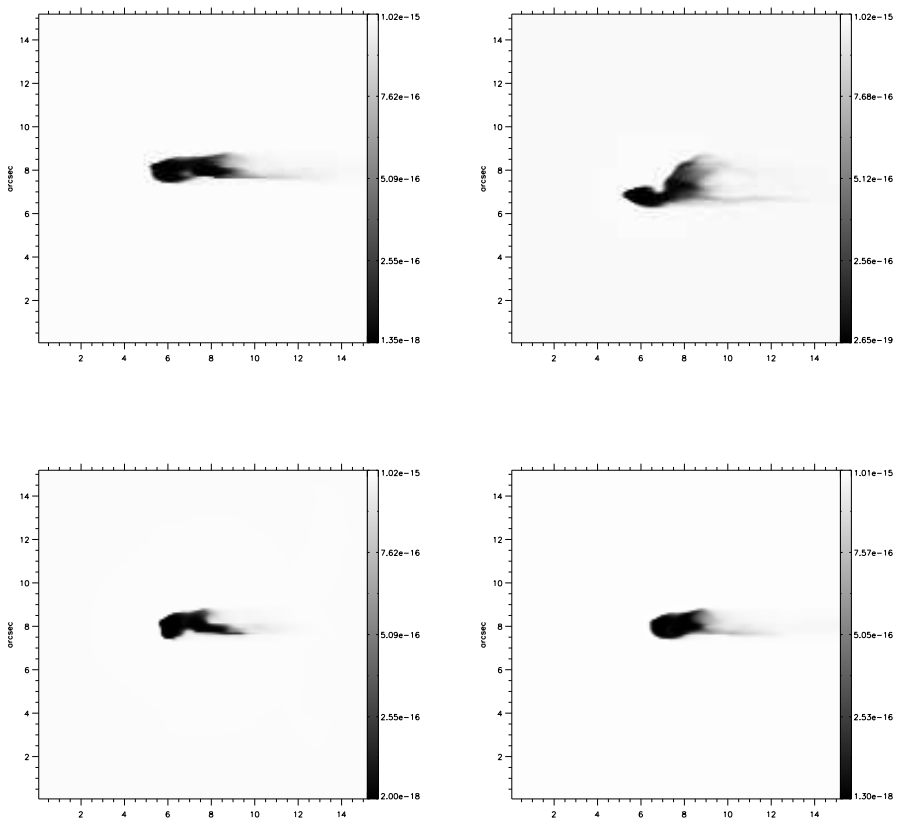

Figure 16: Synthesized Hα images of case A at $t = 20$ kyrs. The ionizing source is to the left in all frames. *Upper left*: side view, x-z plane. *Upper right*: side view, x-y plane. *Lower left*: bright side view , rotated 60° relative to the x-z plane. *Lower right*: cold side view, rotated 45° relative to the x-z plane. The field of view in the image is approximately 15" × 15" or 0.10 pc. The gray scale indicates flux density in ergs cm^{-2} s^{-1} arcsec^{-2}.

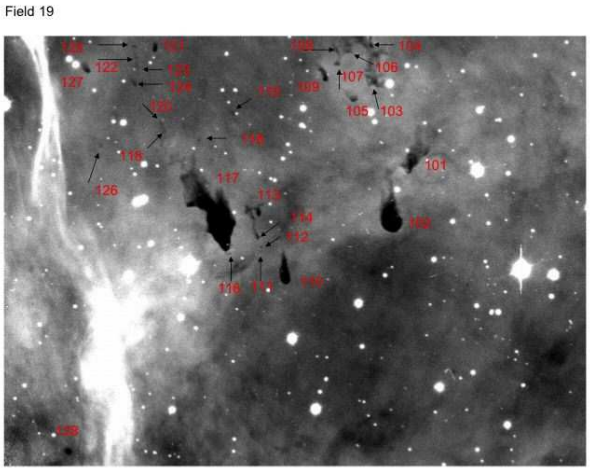

Figure 17: Observed globulettes in a Rosette Nebula field, courtesy of G. Gahm and T. Grenman.

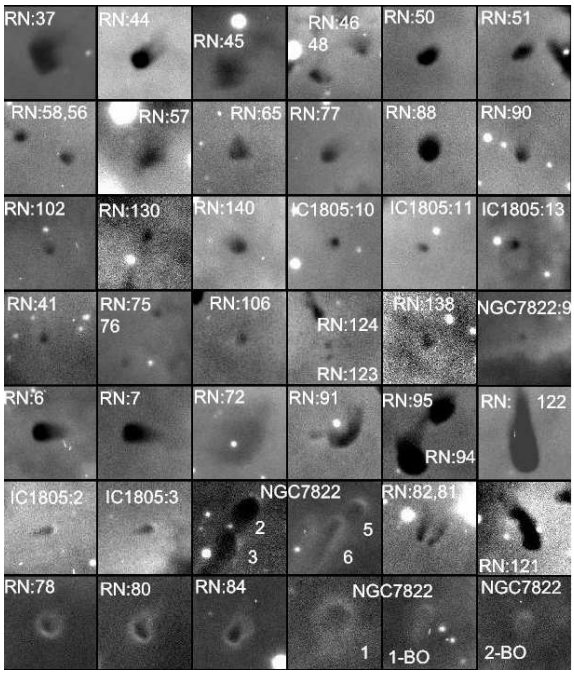

Figure 18: Observed globulettes, reproduced from Gahm et al. (2007). Each image is 17" square, corresponding to 0.12 pc in the Rosette Nebula (RN), 0.20 pc in IC 1805 and 0.07 pc in NGC 7822.

the lifetime of globules as

$$t_{ion} = \left(\frac{L}{10^{17}\text{ cm}}\right) S_{49}^{-1} R_{pc} \left(\frac{n_0}{10^3\text{ cm}^{-3}}\right) \times 38\text{ yrs}, \tag{43}$$

with L as the typical size of a globule, S_{49} as the source rate of ionizing photons in 10^{49} photons s^{-1}, R_{pc} as the distance to the source in pc and n_0 as the average number density. This estimate omits any shielding effects from the evaporation flow and assumes that the cloud does not respond dynamically to the ionizing flux or form an equilibrium cometary cloud, which most likely is an oversimplification for clouds in the Rosette Nebula parameter range. For the simulated case A, setting $L = 1 \times 10^{17}$ cm, t_{ion} amounts to 190 years, which is clearly inconsistent with the numerical lifetimes obtained in this work.

The application of the Mellema et al. (1998) model used in Gahm et al. (2007) assumes that the clouds are in equilibrium and that the scale height of observed clouds can be approximated with $h_0 \approx \bar{r}$, the mean cloud radius. Gahm et al. calculate cloud lifetimes around $t_m \sim 10^6$ yrs, concluding that the free fall time $t_{ff} < t_m$ and that globulettes will have time to collapse if they become gravitationally unstable. However, applying the parameters used in this work, the equilibrium cometary cloud model of Mellema et al. (1998) indicates scale heights that are lower by an order of magnitude than the actual radii of observed clouds in Gahm et al. (2007). Using the parameters of case 1 with an initial equilibrium state mass $M \approx 15 M_{Jup}$, setting $c_1 = 0.34$ km s^{-1}, $c_2 = 10$ km s^{-1}, we obtain an equilibrium peak pressure $p_c/k \approx 3 \times 10^8$ K cm^{-3}, a shielding factor $q = F/F_i \approx 4$ and a scale height $h_0 \approx 6 \times 10^{15}$ cm. This is confirmed by the numerical simulations, as simulated clouds that start out at the observed radii and estimated densities tend to become heavily compressed during the initial implosion. The tendency of fragmentation to occur at shorter length scales than observed globulette radii is also problematic. This failure to match observations might be explained by one or more of the following factors:

1. Observed clouds are not described accurately by the equilibrium cometary state, possibly because they have not yet had time to settle

2. Systematic effects leading to underestimation of cloud masses in observations, e.g. unresolved dense cores

3. Significant contributions to the cloud supporting pressure from non-thermal mechanisms, such as magnetic pressure

4. The implicit assumption that Rosette Nebula globules are cooled efficiently enough to remain at $T \sim 20$ K when shocked may not apply to all cases

5. Projection effects and unresolved structure in observations causing the characteristic scale height, equalling the radius of curvature at the tip of the ionization front, to be overestimated

6. The incident UV photon flux F, which drives the pressure gradient, is overestimated, e.g. because of absorption within the H II region

The temperature model used in this work uses a heating/cooling function source term rather than the two temperature equation of state employed in Esquivel & Raga (2007). The model used here allows for a physically more accurate representation of the temperature evolution of the cloud. However, the internal temperature structure of globules, especially before reaching the equilibrium state, remains uncertain. Because of this uncertainty, the degree to which the cloud is compressed initially might be overestimated.

6.2 Suggestions for future work

The temperature model is crucial to obtain accurate quantitative estimates for the lowest possible cloud masses that might result in formation of dense collapsing objects. Therefore, a detailed study of local heating/cooling factors in the cloud is necessary. To accurately model the internal temperature structure of the cloud, resolving the cooling region and the shocked layer, requires a high grid resolution; however, with the constant cell size model employed here, further refinement of the grid quickly becomes prohibitively expensive. This is due to the fact that in this model, the entire distance moved by the cloud, while being accelerated by the rocket effect, needs to be represented in high resolution. As the required resolution is likely to be considerably lower outside of the cloud, adaptive mesh refinement methods, where the resolution is dynamically refined in regions of interest, would be very useful for the study of internal cloud structure. In order to reduce the required size of the computational grid further, the problem could be reformulated for a co-moving, accelerating coordinate system, removing the need to simulate the entire distance traveled by the cloud at all times.

The initial state of the globule in the simulation mimics the analytical model, neglecting self-gravity. While being numerically complex, including self-gravity in the model is necessary to provide an accurate description of possible central collapse. Additionally, it would allow the simulations to start out with a centrally condensed sphere in hydrostatic equilibrium, which is closer to a realistic situation. The methods employed in this work are indirect and only valid up to the point where gravity becomes non-negligible. Probing the lower size limit of objects formed in photo-evaporating clouds requires some form of gravitational model.

Due to globulettes being defined by their size close to the lower observational limit, the morphology and internal structure of small globulettes in the Rosette Nebula and similar regions is somewhat uncertain. A survey

of the temperature properties of small globules could be used to improve the current temperature model and yield better estimates of the supporting pressure. Observations resolving centrally condensed globulettes, or observations of globulettes containing low luminosity IR objects, would indicate that these have been highly compressed during earlier evolution stages and that planetary mass or low stellar mass objects may form in this process, which in turn constrains lifetime estimates.

Accurate photometry of the emission from recombination lines in the bright rims of Rosette Nebula globulettes might be used in combination with other observationally determined properties to independently estimate the ionizing UV photon flux in the rim; a significantly lower flux estimate than the one used here, $F = 1.44 \times 10^{50} \ /(4\pi R^2)$ photons cm^{-2} s^{-1}, would help in explaining the apparent discrepancy between the equilibrium sizes predicted by the model and the observed sizes.

7 Conclusions

The numerically obtained timescale in this work for the total photo-evaporation of globulettes is 5×10^4 years. This confirms the earlier picture that cometary globules can resist ionization for a long time, remaining inside the H II region. At the same time, they are accelerated outwards due to the initial shock and the rocket effect from the evaporation flow, moving considerable distances before evaporating completely.

Indications on gravitational collapse remain somewhat inconclusive, because while the coolest parts of the cloud might be inclined to contract gravitationally during the initial implosion if they are cold enough, the uncertainty in determining the cloud temperature at the point of highest compression leads to a corresponding uncertainty in the collapse criteria, as $M_{BE} \propto T^2$. For clouds in the stellar mass range similar to the simulated case C, it seems that gravitational effects must be taken into account during the implosion phase. However, there is no indication of globulettes that have reached the equilibrium cometary cloud state becoming gravitationally unstable, unless they have already formed a collapsing core when initially compressed. Consequently, it seems unlikely for 10 M_{Jup} globulettes in such equilibrium to form dense planetary mass objects, unless they can be shown observationally to already contain embedded collapsing cores.

8 Acknowledgements

First and foremost, my advisor Garrelt Mellema deserves a great thank you for the time he has spent guiding me into this field and all the work spent on the CAPREOLE code. Also, I would like to thank Gösta Gahm and his collaborator Tiia Grenman for providing their observational data and

analysis in addition to many valuable suggestions and enlightening discussions. Many thanks to Sergio Gelato for his patience with my questions, some of them annoyingly trivial I fear, and for the generous access to the department's computing resources. There are numerous other staff and fellow students at the department who at some point or another during this work have contributed to my understanding of the field or taught me a few tricks, including, but not limited to; Göran Olofsson, René Liseau, Jacob Trier Fredriksen, Milan Battelino, and Jeanette Bast. And of course, last, but not least, my beloved, the amazingly talented Elin, whose opinions I've always valued dearly, and who supports everything I do in countless ways. Thank you.

References

[1] Bertoldi, F., 1989, AJ **346**, 735

[2] Bertoldi, F. & McKee, C. F., 1990, AJ **354**, 529

[3] Celnik, W. E., 1983, A&A Suppl. Ser. **53**, 403

[4] Celnik, W. E., 1985, A&A **144**, 171

[5] Cerqueira, A. H., Cantó, J., Raga, A. C. & Vasconcelos, M. J., 2006, Revista Mexicana de Astronomía y Astrofísica **42**, 203

[6] Cox, P., Deharveng, L. & Leene, A., 1990, A&A **230**, 181

[7] Dalgarno, A., McCray, R. A., 1972, Ann. Rev. of Astron. & Astroph. **10**, 375

[8] De Marco, O., O'Dell, C. R, Gelfond, P., Rubin, R. H. & Glover, S. C. O., 2006, AJ **131**, 2580

[9] Dyson, J. E., 1968, Ap. Space Sci. **1**, 388

[10] Dyson, J. E., 1973, A&A **27**, 459

[11] Esquivel, A., Lazarian, A., Pogosyan, D. & Cho, J., 2003, Mon. Not. R. Astron. Soc. **342**, 325

[12] Esquivel, A. & Raga, A.C., 2007, Mon. Not. R. Astron. Soc. **377**, 383

[13] Gahm, G. F., Grenman, T., Fredriksson, S. & Kristen, H., 2007, AJ **133**, 1795

[14] González-Alfonso, E. & Cernicharo, J., 1994, AJ **430**, L125

[15] Grenman, T., 2006, Licentiate thesis, Luleå University of Technology (ISSN 1402-1757)

[16] Lefloch, B. & Lazareff, B., 1994, A&A **289**, 559

[17] Leung, C. M., 1985, in *Protostars and Planets II*, ed. D. C. Black & M. S. Matthews (Tucson: Univ. Arizona Press), 104

[18] Mellema, G., Eulderink, F. & Icke, V., 1990, A&A **252**, 718

[19] Mellema, G., Raga, A. C., Cantó, J., Lundqvist, P., Balick, B., Steffen, W. & Noriega-Crespo, A., 1998, A&A **331**, 335

[20] Mellema, G., Iliev, I. T., Alvarez, M. A. & Shapiro, P. R., 2006, NewA **11**, 374

[21] Ogura, K. & Ishida, K., 1981, Publ. Astron. Soc. Japan **33**, 149

[22] Oort, J. H., Spitzer, L., 1955, ApJ **121**, 6

[23] Osterbrock, D.E., 1989, *Astrophysics of Gaseous Nebulae and Active Galactic Nuclei* (Mill Valley, CA : University Science Books)

[24] Reipurth, B., Raga, A. & Heathcote, S., 2003, AJ **126**, 1925

[25] Stahler, S.W., Palla, F., 2004, *The Formation of Stars* (Weinheim, Germany: Wiley-VCH Verlag GmbH & Co. KGaA)

[26] Vacca, W. D. , Garmany, C. D. & Shull, J. M., 1996, ApJ **460**, 914